A Novel P-Q Control Structure for Interleaved Full Bridge Converter in a Multifunctional Single-Phase AC Battery Application

Tuan Anh Do[1,2], Quang Dich Nguyen[2], Phuong Vu[1‡]

[1]School of Electrical & Electronic Engineering, Hanoi University of Science and Technology, No. 1, Dai Co Viet, Hai Ba Trung, Ha Noi 100000, Viet Nam

[2]Institute for Control Engineering and Automation, Hanoi University of Science and Technology, No. 1, Dai Co Viet, Hai Ba Trung, Ha Noi 100000, Viet Nam.

(anh.dotuan1@hust.edu.vn, dich.nguyenquang@hust.ed.vn, phuong.vuhoang@hust.edu.vn)

‡ Corresponding Author: Phuong Vu, School of Electrical and Electronic Engineering, Hanoi University of Science and Technology, Hanoi; phuong.vuhoang@hust.edu.vn

Received: 16.01.2024 Accepted: 06.03.2024

Abstract- Recently, the home battery has been of research interest as a sustainable energy storage system for solar self-consumption, time-based control, and backup. This research focuses on the fully integrated AC Battery, a typical home battery with an AC-coupled topology, which typically consists of two-stage power conversion. First, the Interleaved Full Bridge (IFB) converter is proposed for the Power Factor Correction (PFC) stage in a single-phase system, owing to its advantages of reduced current stress and lower output current ripple. Secondly, one important task of a multi-functional AC Battery is to independently control active and reactive power, thereby supporting the grid in supplying power to domestic loads. Therefore, this paper proposes a single-phase PQ control scheme for the IFB converter to achieve this task, with the battery power delivered through the DC/DC stage treated as an adjustable current source. Thirdly, the orthogonal current generated by a fictive-axis emulator (FAE) is applied for the proposed control structure for the IFB converter, which improves the dynamic response of the current regulator and the overall system. To quickly verify the advantages of the IFB converter and the proposed control structure, real-time simulation on the Typhoon Hardware-in-the-loop (HIL) platform is conducted across several scenarios: active power compensation, power factor compensation, and Point of Common Coupling (PCC) voltage regulation. The simulation results validate the effectiveness of the control structure for the proposed converter in an AC Battery application.

Keywords Multi-functional single-phase AC battery, power factor correction stage, interleaved full bridge converter, PQ control, fictive-axis emulator.

1. Introduction

By 2030, Electric Vehicles (EVs) are expected to completely replace traditional gasoline-powered cars to achieve the zero-net-emissions goal, as discussed at the COP-26 conference [1]. The proliferation of EV adoption has led to increased attention to EV batteries, particularly when they reach 70–80% of their original capacity and are no longer suitable for automotive use [2]. These batteries, referred to as Second-Life Batteries (SLBs), are increasingly being reused in Battery Energy Storage Systems (BESS) and other applications [3]. In this field, a notable application is home battery storage systems (or home batteries) [4-5], which exchange energy with various household sources, such as grid power, renewable energy, EV batteries, and loads, through a power-converter system. This study specifically focuses on the AC-coupled configuration of home batteries due to its flexible integration with existing home photovoltaic (PV) systems, the isolation of the battery pack, and its potential for expansion with additional modules. Notably, many well-known manufacturers have recently introduced the AC Battery [6-8], a system that integrates the battery and power converters, and there is a growing trend toward incorporating multiple modules.

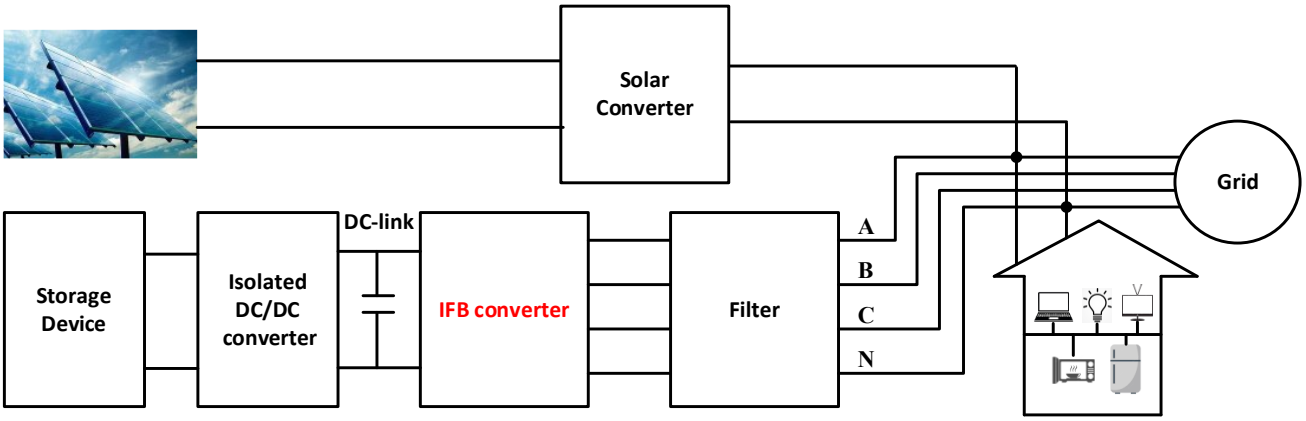

Fig. 1. Structure of a home battery application using a 3-phase CFDAB converter.

Because second-life batteries are used in the AC Battery in this research, a power rate of 11kW is selected, consistent with the Level 2 charging standard for an On-Board Charger for the initial batteries. The two-stage topology in Fig. 1, comprising an isolated DC/DC stage and a PFC stage [9-13], is chosen for the flexible application of the AC Battery, with the PFC stage being the focus of this paper. The ability to provide 3-phase grid power across different regions and the required battery power rate in the system affect the structure of the PFC converter in an AC Battery. In the US and some countries, only single-phase grids are available, and the charging power rate for EVs can reach up to 11kW. At the power rate of 6.6kW, the Totem-Pole structure achieves the best performance according to the TI design [14]. However, increasing the power to 11kW significantly increases current ripple and current stress, leading to bulky passive components, higher losses, and increased electromagnetic noise.

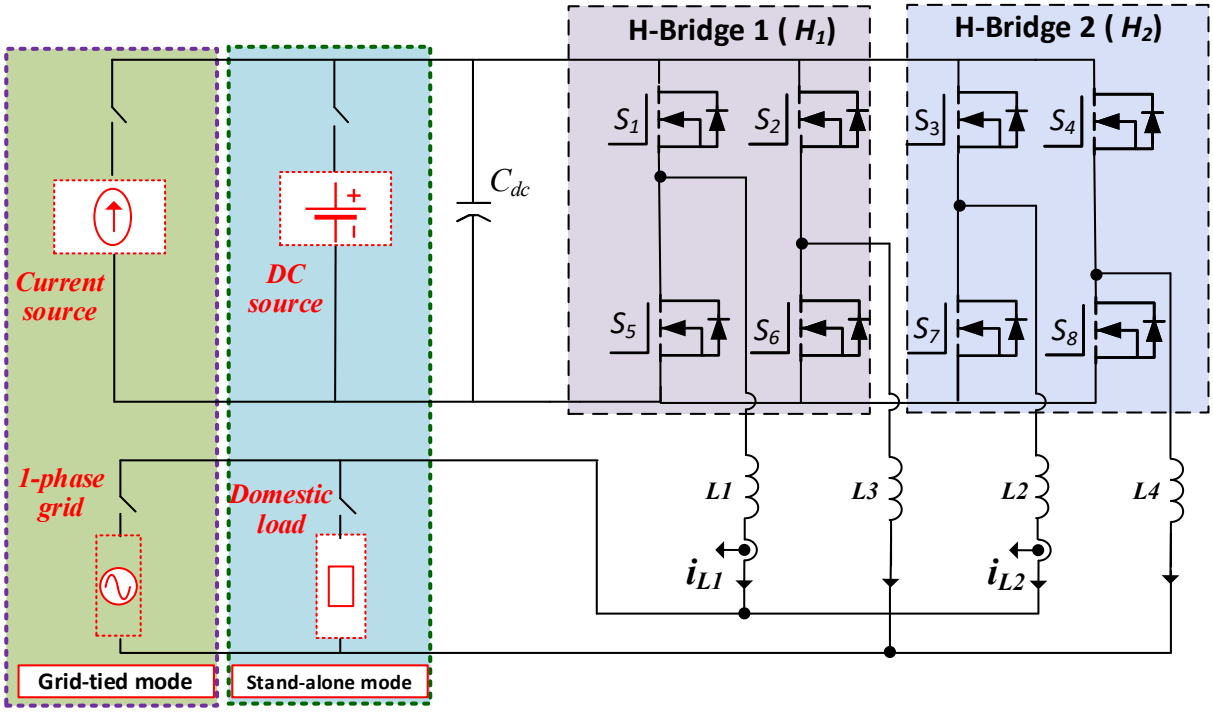

Fig. 2. Overall structure of IFB converter in multiple modes in an AC Battery application.

The Interleaved Full Bridge (IFB) [6,7] structure offers significant advantages, including reduced current stress and output current ripple, as well as reduced Electromagnetic Interference (EMI). This structure could eliminate the high-frequency component of the common-mode voltage, thereby mitigating leakage current. Moreover, the IFB structure is adaptable and can be readily modified to operate in both single- and three-phase grid systems, making the AC battery compatible with diverse regions. To operate a multifunctional AC Battery system, reactive and active power must be

controlled independently. The P-Q theory on the dq coordinate axis system has long been widely applied to three-phase systems with various applications such as active filters [15], AC drives[16], microgrid systems [17], and distributed renewable energy systems [18]. Subsequently, this theory has been extended to single-phase systems as a PQ control scheme, or vector control [19-20]. Subsequently, various methods have been proposed to compute the average values of active and reactive power for single-phase grid-connected inverters [21].

In the common approach, the orthogonal imaginary quantities in PQ control are obtained by phase-shifting the real components by a quarter of the fundamental period. The introduction of such a delay in the system deteriorates the dynamic response, which becomes slower and oscillatory [22]. To solve this, the orthogonal quantities in [22] are generated by an imaginary system called a fictive axis, which runs concurrently with the real one. This approach is referred to as the fictive-axis emulation (FAE) method, effectively improving the poor dynamics of the conventional one.

This paper proposes a new P-Q control strategy for the IFB converter in an AC Battery application. The proposed control structure is implemented in the synchronous frame to control the active and reactive power independently. Furthermore, the FAE method is applied to achieve a faster dynamic response. Finally, to quickly verify the effectiveness and feasibility of the control method, real-time simulation is conducted across various scenarios: active power compensation, power factor compensation, and PCC voltage regulation. The simulation results prove the effectiveness of the proposed control structure.

2. Proposed Control Structure for IFB Converter

2.1. Operational Principle of the IFB Converter with the Interleaved Bipolar Pulse Width Modulation (IB-PWM) Method

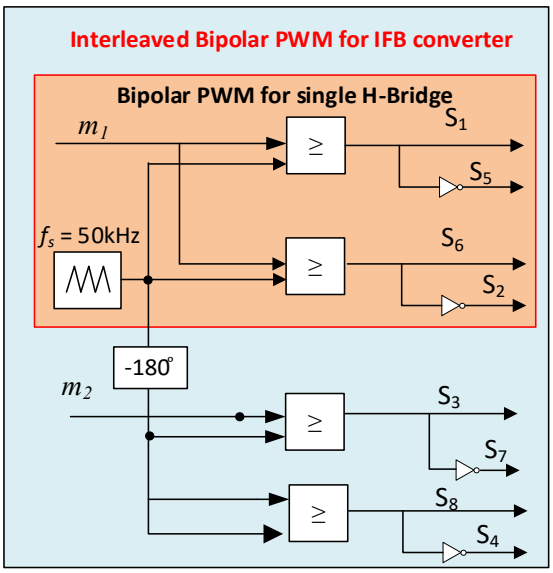

Fig. 3. Pulse diagram of the IB- PWM method.

In this section, interleaved bipolar PWM modulation is defined for the IFB converter. The structure of the IFB converter is shown in Fig. 2. Switches S_1, S_2, S_5, and S_6 are in the first H-Bridge (H_1), two branches connected to two split-inductors L_1 and L_2 are symbolled as branch 1 and branch 2, respectively. Similarly, switches S_3, S_4, S_7, and S_8 belong to the second H- Bridge (H_2) with branch 3 and branch 4 connecting to two split inductors L_3 and L_4, respectively.

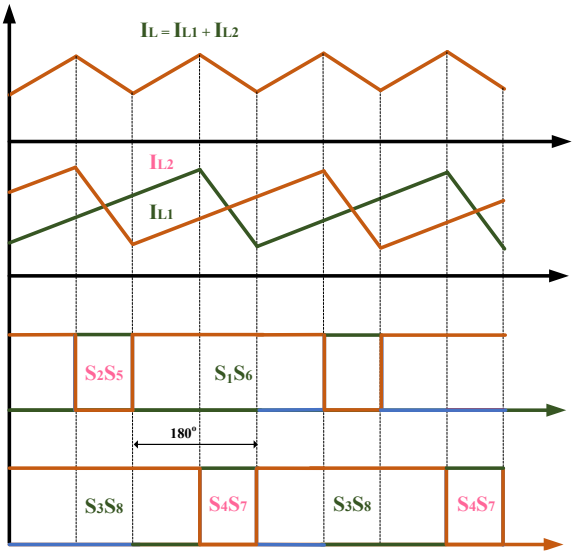

b)

Fig. 4. Typical pulse pattern of the IFB converter applied to the IB-PWM method.

The Bipolar PWM technique for an H-Bridge converter uses a modulation signal to compare with a single carrier. This paper applied the Interleaved Bipolar PWM method to the IFB converter, keeping the phase difference between the two carriers of the two H-Bridges exactly 180 degrees, as shown in Fig. 3. The corresponding pulse pattern of the IB-PWM for the IFB converter is presented in Fig. 4 for 4 modes.

2.2. FAE Algorithm

The single-phase PQ control structure technique for the IFB converter is applied as shown in Fig. 4, in which the FAE method generates the imaginary orthogonal converter current. The β - component of the PCC voltage and β - component of the output of the current controller is the input of the FAE module. The symbol 'x' represents the signal of the corresponding H-bridge. With the detailed diagram in Fig. 4, the β - component of the converter current is obtained. This orthogonal current and the converter current are then fed into a dq current regulator. Therefore, upon step changes in the d or q reference values, the actual quantities in the real and *imaginary* systems react at the same time and in the same way to track the reference quantities. This contrasts with common approaches in which the imaginary component lags the real component by a quarter cycle, which explains the relatively poor dynamic response of conventional dq control strategies in single-phase converters.

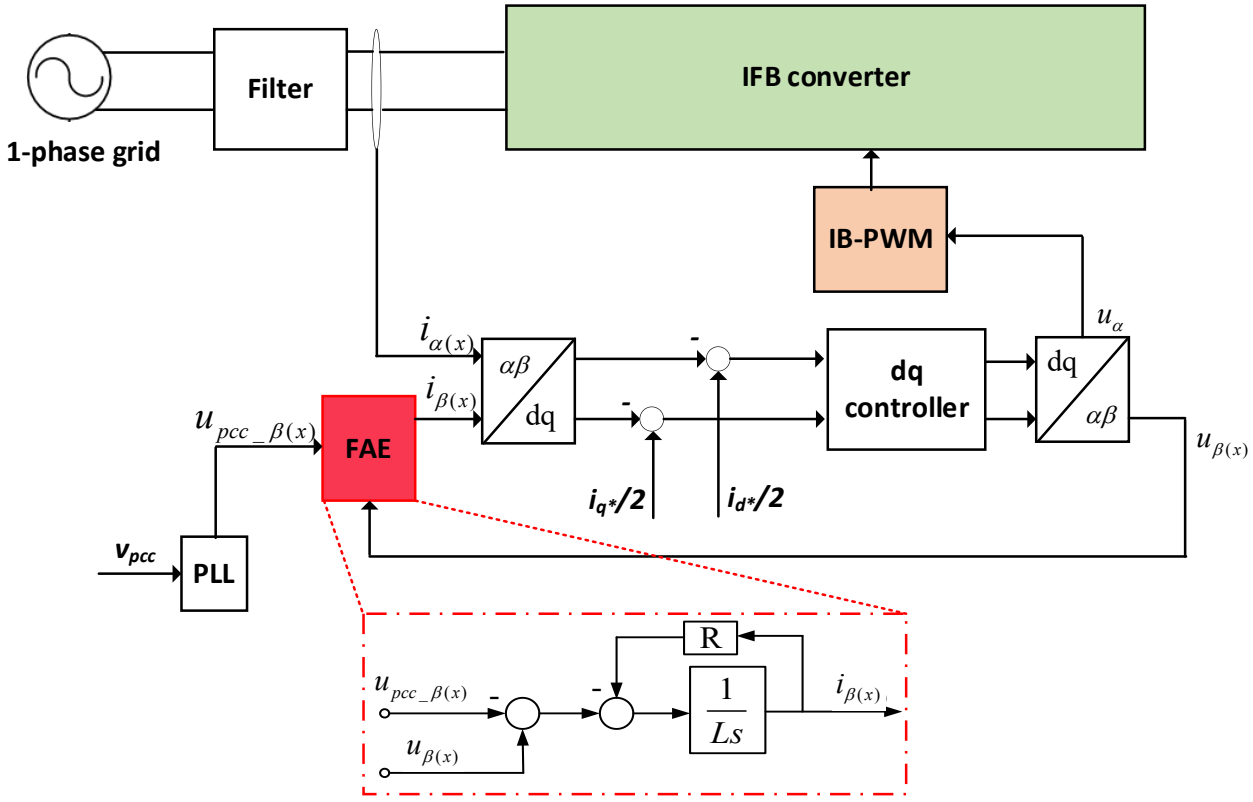

Fig. 5. Fictive axis emulator technique.

After that, the measured current i_α and current on the fictive axis undergo the Park transformation to obtain the current on the synchronous frame i_d and i_q. These currents serve as feedback to the current controllers.

2.3. Active Power Compensation

The proposed control structure for the IFB converter AC Battery for the active power compensation function is depicted in Fig. 5. In this mode, the circuit comprises the IFB converter connected to the grid and the domestic load via an LC filter. At the same time, the DC-side current source (I_{dc}) represents the required active battery power P_{bat} controlled by the DC/DC converter. Defining the DC-link voltage as U_{dc}, the current source can then be determined as follows:

$$I_{dc} = \frac{P_{bat}}{U_{dc}} \tag{1}$$

The active power and reactive power will be controlled independently through the d-axis current i_d and the q-axis current i_q, respectively. The feedback signal of the DC voltage is filtered with a notch filter to eliminate the 100 Hz oscillating component, and the id is then derived from the output of the DC voltage controller. Assuming that the currents through four split-inductors are balanced, the reference d-axis current for each H-bridge is equal to half of the reference I_{d*}. In the active power compensation scenario, the q-axis reference component is set to zero. The feedback currents i_d and i_q are computed using the Park transformation and the FAE technique described above. The symbol '*x*' represents the signal of the corresponding H- Bridge (x = 1 for H-Bridge 1 and x = 2 for H- H-Bridge 2). Moreover, the design of the current controller for each H-Bridge and the DC voltage controller is similar to the traditional approach [22]. Finally, the Interleaved Bipolar PWM (IB-PWM) is applied to generate the control signal for the IFB converter. In this configuration, the load's demanded active power is measured from the PCC voltage, vpcc, and the load current, i_{Load}. Assuming grid power is limited, the compensated active power is supplied by the battery, which can be modeled as a current source at the DC link. The compensated current source in this scenario is formulated as follows:

$$I_{dc} = \frac{P_{load} - P_{grid\_\max}}{U_{dc}} \tag{2}$$

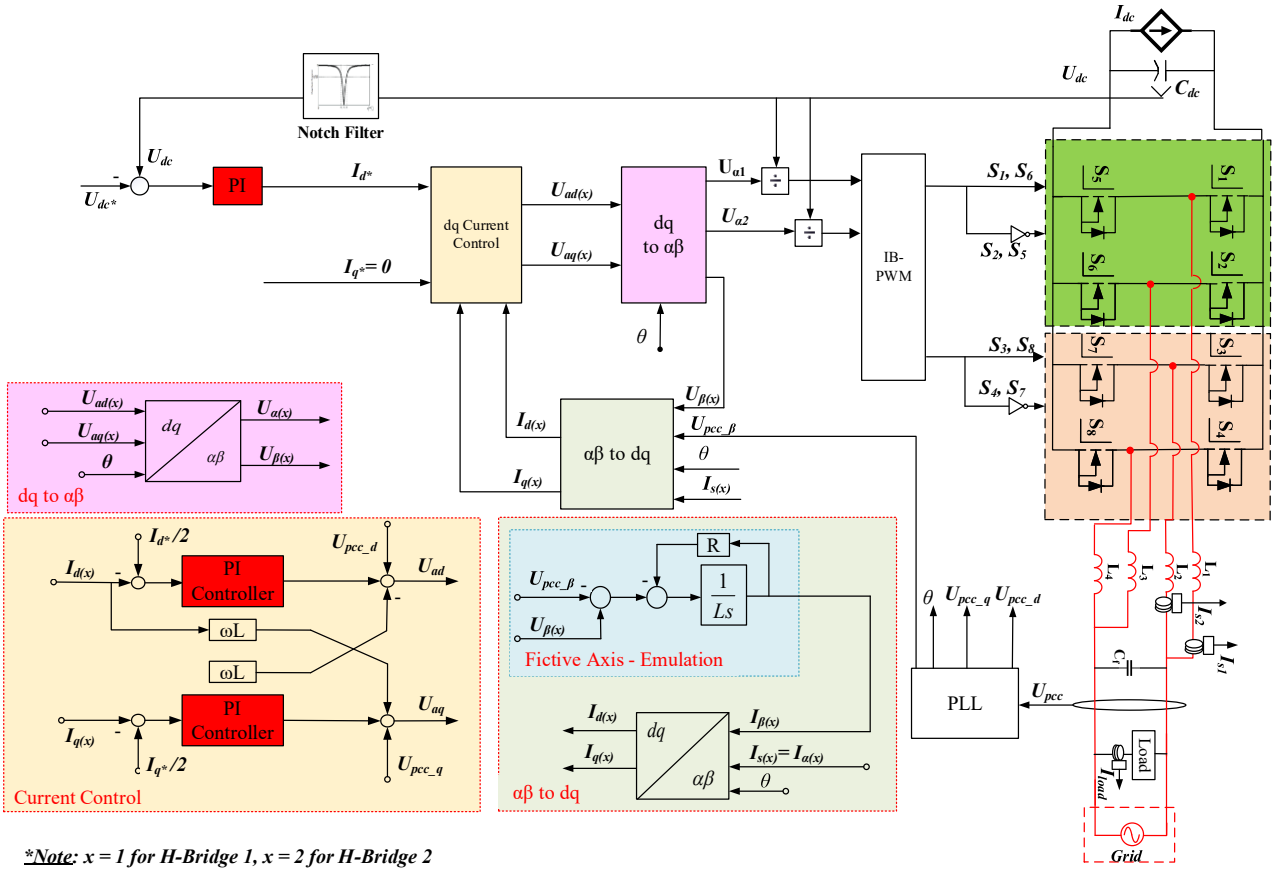

Fig. 6. Control structure for active power compensation.

2.4. Reactive Power Compensation

The control structure of the IFB converter in grid-connected mode for the AC Battery's reactive power compensation function is depicted in Fig. 6, which features two control loops, including the aforementioned active power compensation loop. The FAE technique is still applied to improve the dynamic response, while the IB-PWM helps achieve lower current ripple and lower Total Harmonic Distortion (THD) of the grid current. However, in this scenario, the q-axis reference current, rather than being set to zero, is calculated from the compensated reactive power in two cases: improving the power factor or regulating the PCC voltage.

2.4.1. Power factor compensation

While a conventional unidirectional system can provide only reactive power before the battery is fully charged [23], a bidirectional system, such as the proposed multi-functional AC Battery, addresses this limitation. The required reactive power is supplied by the DC-link capacitor, not the battery, thereby reducing stress on the battery. This consequently extends the battery's lifespan, which is particularly important for second-life batteries.

The demanded reactive power is equal to the reactive power of the load, which is calculated from the PCC voltage v_{PCC} and the load current i_L as follows [24]:

$$Q_{ref1} = \frac{|v_{pcc}|}{\sqrt{2}} \times \frac{|i_L|}{\sqrt{2}} \times \sin(\angle v_{pcc} - \angle i_L) \tag{3}$$

From that, the total q-axis reference current value I_{qr*} is calculated from the d-component of the PCC voltage V_{pccd} :

$$I_{qr} = \frac{2Q_{ref1}}{V_{pccd}} \tag{4}$$

Assuming that the currents through four split-inductors are balanced, the reference q-axis current for each H-bridge is equal to half of the reference I_{qr*}.

2.4.2. PCC voltage regulation

The simplified diagram of the distribution grid in Fig. 8 consists of the grid, distribution transformer, transmission line, and the IFB converter for the PFC stage.

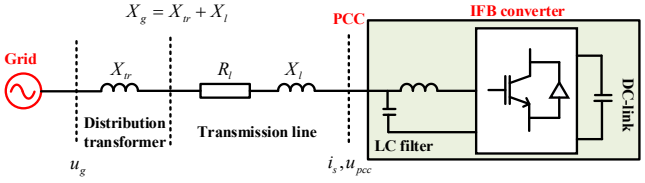

Fig. 7. Simplified model of a grid-tied system.

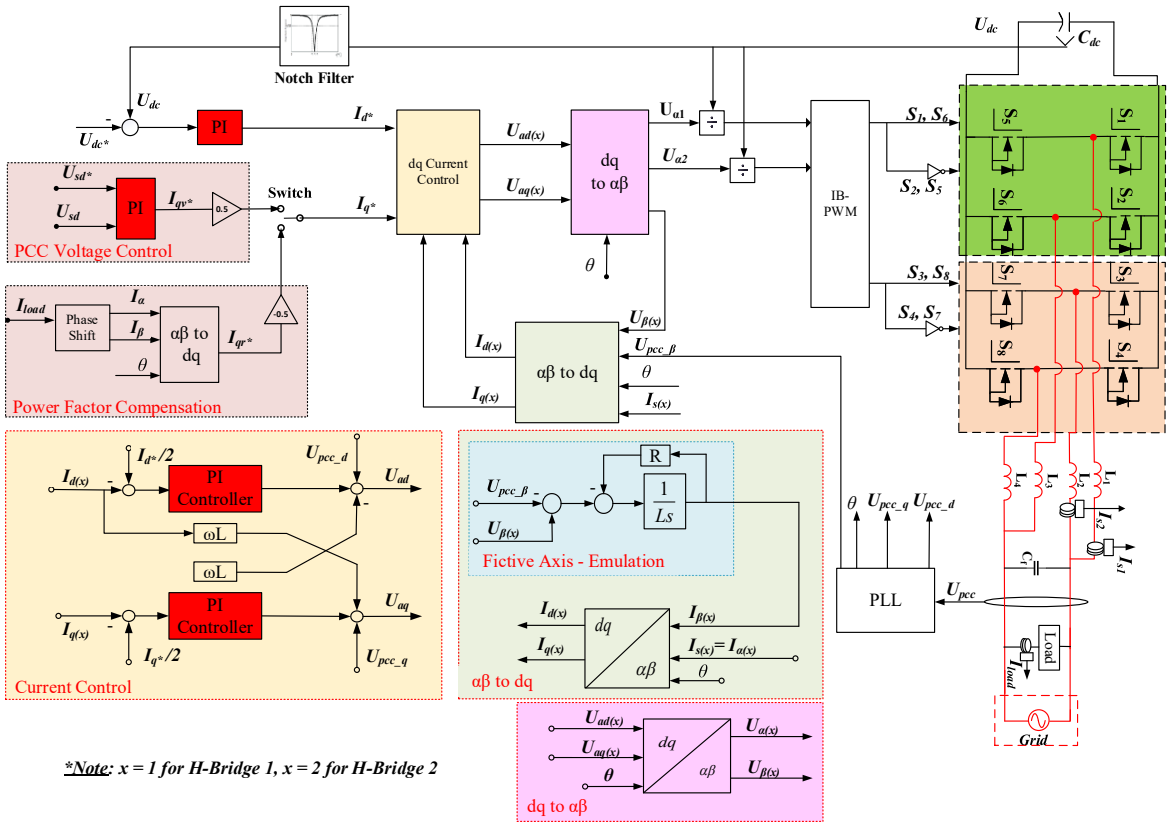

Fig. 8. Control structure for reactive power compensation.

The root-mean-square (RMS) values of the grid voltage, PCC voltage, and the voltage drop across the line impedance are V_g, V_{PCC}, and ΔV, respectively. The PCC voltage drop can be calculated from the line impedance, the active and reactive power of the grid [25]:

$$\Delta V = \frac{P_g R_g + Q_g X_g}{V_g} \tag{5}$$

PCC voltage regulation is achieved by controlling reactive power between the PFC converter and the grid. As with power factor compensation, the required reactive power is supplied by the DC-link capacitor on the PFC side. Because the PCC voltage can be easily monitored, a local approach that detects variations in PCC voltage amplitude is presented in [24]. The converter then injects or absorbs reactive power based on the voltage difference. This method is particularly suitable for an AC Battery in a residential application, which doesn't require additional communication infrastructure.

Eq. (5) indicates that the PCC voltage depends on both the grid active and reactive power. Therefore, the DC voltage controller and PCC voltage controller are dynamically coupled. Since it is difficult in practice to measure or estimate the grid impedance, the response time of the PCC controllers is chosen to be 10 times slower than that of the DC voltage controller [24]. Moreover, Phase-Locked Loops (PLLs) offer significantly faster response times than DC voltage controllers; hence, the dynamics of PLLs do not affect the PCC controllers. From the simplified model of the system, the PCC voltage control loop is designed in [26] as shown in Fig. 9. $G_c(s)$ represents the current loop, and because its response time is much faster than that of the PCC controller loop, it can be considered that $G_c(s) = 1$:

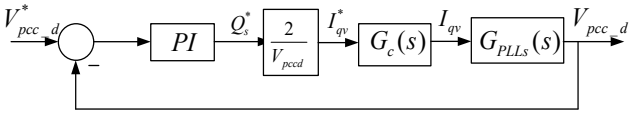

Fig. 9. Control structure for the PCC voltage.

In which the object transfer function of the PCC controller:

$$G_{PLL}(s) = \frac{\Delta V_{pcc\_d}}{\Delta I_{qv}} = -\omega L_T \tag{6}$$

To achieve zero steady-state error, the PCC voltage controller requires an open-loop transfer function with at least one pole near the origin. To achieve this goal, an integrator with a scalar gain, suitable for the PCC voltage controller [25], is employed in this paper. The output of the PI controller is defined as Q_{ref2}, then the reference current I_{qv*} could be calculated as:

$$I_{qv*} = \frac{2Q_{ref\,2}}{V_{pccd}} \tag{7}$$

3. Real-Time Simulation Verification

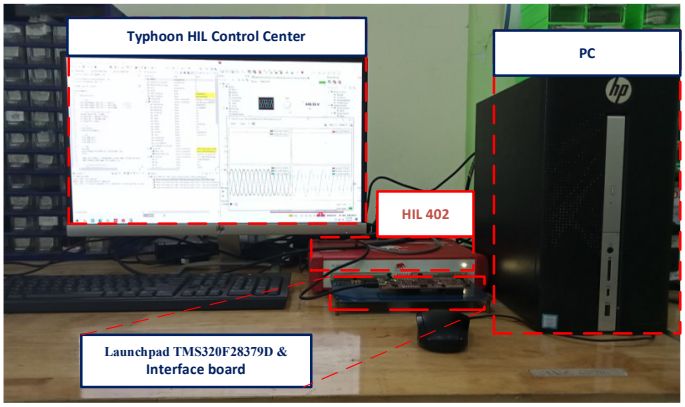

Fig. 10. Real-time simulation system.

Table 1. Simulation parameters of the IFB converter

	Parameter	Symbol	Value
IFB	Switching frequency	F_{sw}	50 kHz
	Filter inductor	L_i	330 μH
	Internal resistor	r_L	0.1 Ω
	Filter capacitor	C_f	20 μF
	DC capacitor	C_{DC}	1000 μF
GRID	Line voltage	u_g	220 V
	Line frequency	f_g	50 Hz

To quickly verify the PQ control scheme for the three-phase IFB converter, real-time simulation on a HIL platform is conducted, as shown in Fig. 10. In this setup, the IFB converter in grid-connected mode is implemented on a Typhoon HIL 402 device, and the control design is programmed on a TMS320F28379D C2000 DSP kit. An interface board is set up to connect these two devices. The system parameters are given in Table 1.

3.1. PWM Method Comparison

In this scenario, two modulation techniques are compared for the IFB converter: the Interleaved Bipolar-PWM (IB-PWM) method and the Parallel Bipolar-PWM (PB-PWM) with phase differences of 180° and 0° between the two H-bridges, respectively.

Fig. 11 illustrates the advantages of the IB-PWM method compared to the conventional PB-PWM. The split-inductor current ripple of both methods is similar (6A) at the same power rate of 11kW. However, while the grid current ripple with the conventional PB-PWM doubles (12A), the current ripple with IB-PWM significantly decreases to 4A. This leads to a substantial reduction in Total Harmonic Distortion (THD) of the grid current. The THD current of the IB-PWM method is just 2.15%, which meets the IEEE-519 standard and is much smaller than that of the PB-PWM method at 7.93%.

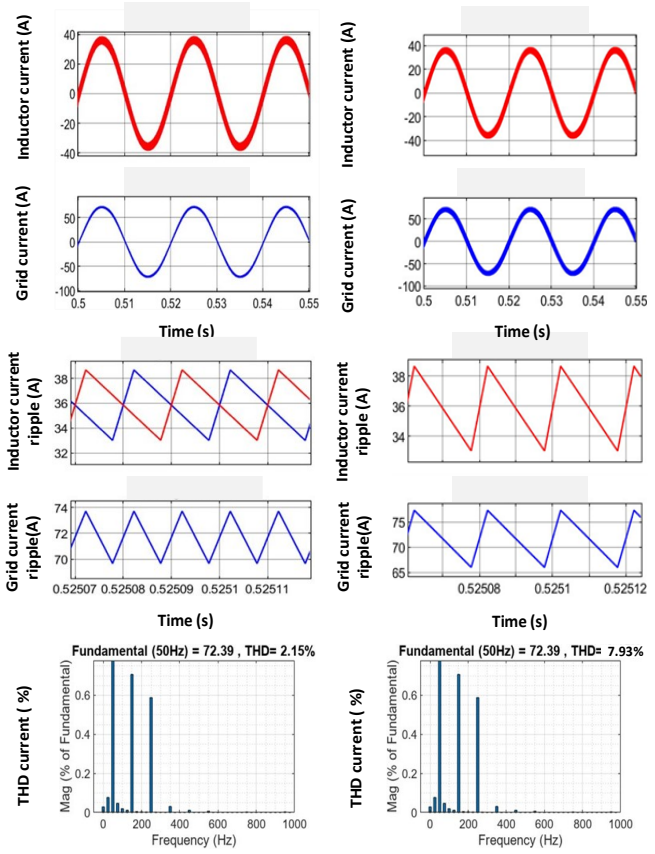

a, Interleaved Bipolar PWM b, Parallel Bipolar PWM

Fig. 11. Current ripple and THD current comparison.

3.2. FAE verification

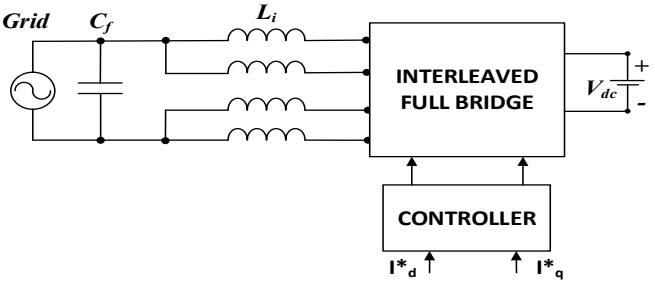

Fig. 12. System diagram for the FAE technique.

Next, the advantage of the FAE method for generating the current, compared with the conventional 90-degree delay

method, is verified when applied to the IFB converter. To evaluate the current dynamic response, the current loop on the synchronous frame is simulated using the system diagram shown in Fig. 12, with simulation parameters similar to those presented in Table 1.

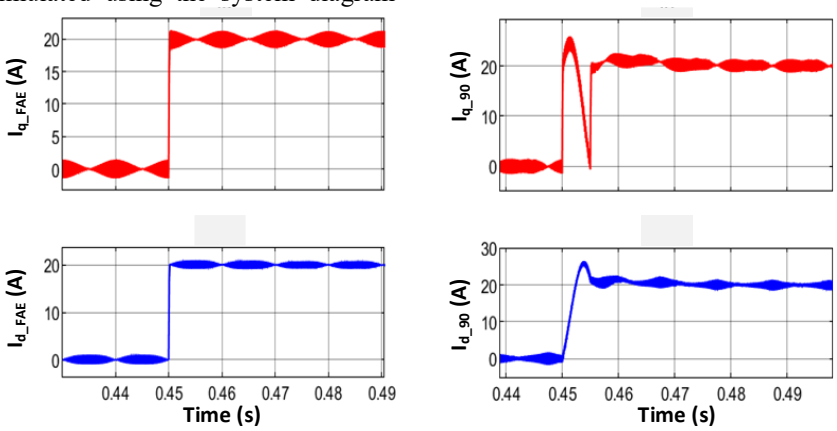

a) *b)*

Fig. 13. Dynamic current response with: a) FAE method, b) Conventional method.

The dynamic responses of the FAE method and the conventional method are compared in Fig. 12. At 0.45s, both references for the d-axis and q-axis current step up from 0 to 20A. As seen in Fig. 13, while the current i_q with the FAE method almost immediately tracks the reference value with no overshoot, the current i_q with the conventional method tracks the reference value after half of the grid cycle with a peak of 25A. The instantaneous response time with no overshoot is also achieved for the current i_d with the FAE method. In contrast, the conventional method requires approximately half a grid cycle for settling and exhibits a 26A overshoot. Given the significant advantages of the FAE technique applied to the IFB converter, the following control structure will be tested for each specific function.

3.3. Active Power Compensation

The system diagram is presented in Fig. 14 and consists of a weak grid with a power rating of 9kW and a resistive load of 20kW; the parameters of the IFB converter and filters are shown in Table 1.

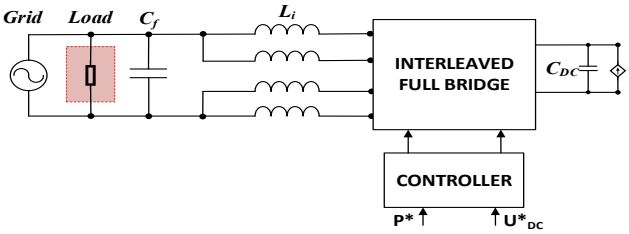

Fig. 14. System diagram for active power compensation.

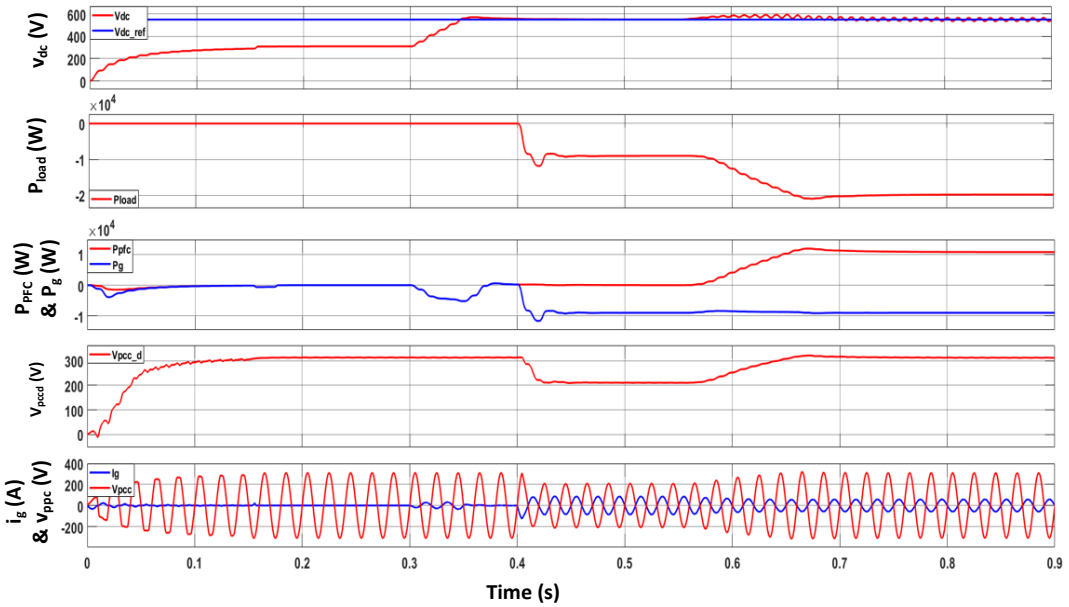

Fig. 15. System responses in the active power compensation scenario.

The simulation results for the active power compensation scenario are presented in Figs. 15 and 16. Overall, the system responses in Fig. 14 comprise 4 stages. In the first stage, from 0 to 0.3s, the DC capacitor is charged through the resistor by the rectifier, and the PLL module extracts the phase of the grid voltage. At 0.3s, the DC voltage controller is started. At this moment, the converter operates at the no-load condition. The negative grid active power in Fig. 15, peaking at 4000W, is used to boost the DC voltage to the reference value. The DC voltage tracks the reference signal and then ramps from 311 VDC to 550 VDC. An overshoot in the DC voltage response is shown in Fig. 15, with a peak of 572V and a response time of approximately 0.1 s.

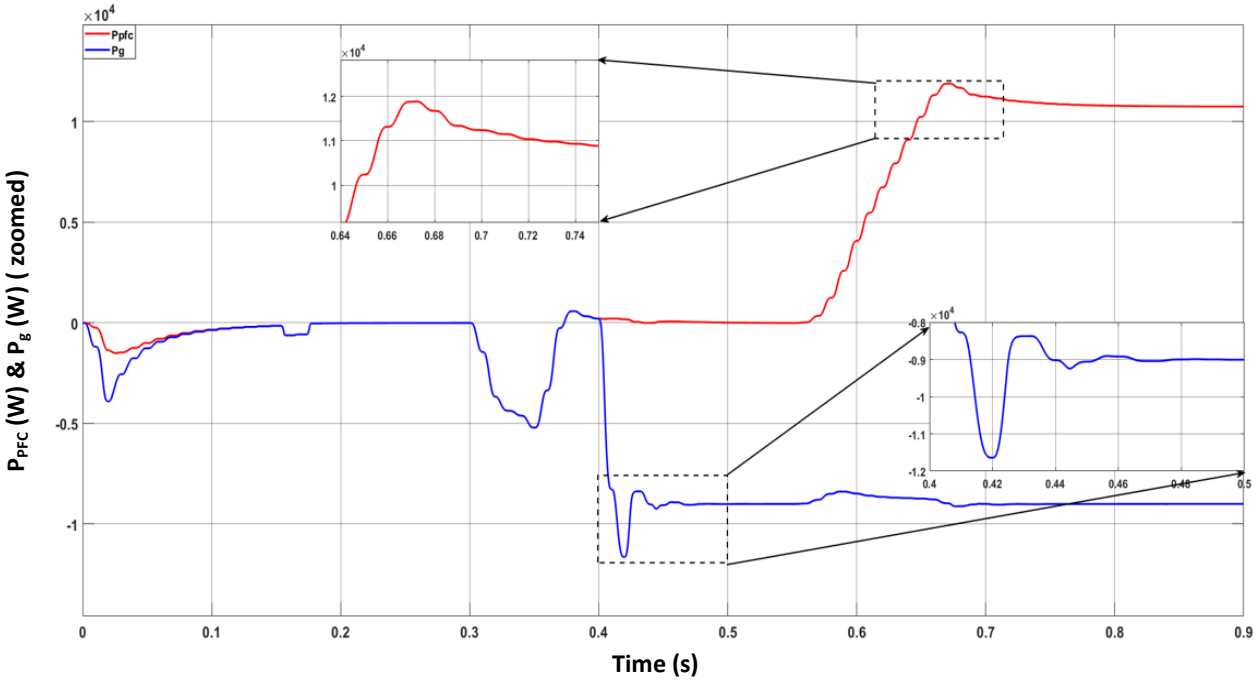

Fig. 16. Active power of the grid and the PFC converter in the active power compensation scenario.

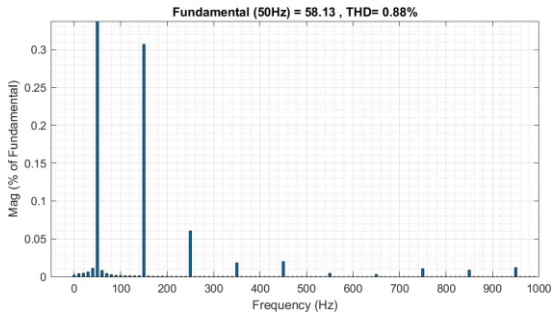

Fig. 17. THD current for active power compensation.

Next, at 0.4s, the resistive load of 20kW is set, which exceeds the weak grid's 9 kW limit. At this time, the grid current has a root-mean-square (RMS) value of approximately 63A, and the grid voltage has dropped to 145V due to insufficient power supply for the load. The voltage V_{pccd} obtained from the PLL block also decreases from 311V to around 200V, as shown in the Fig. 15.

At 0.55 seconds, the IFB converter begins to compensate for active power, with the current source Idc set at the DC-bus according to Eq. (2). The active power provided by the PFC converter reaches 11kW within 0.1 seconds, as shown in Fig. 15, demonstrating the fast dynamic response of the FAE method. At this time, the load in Fig. 16 is adequately supplied with 20kW, with the active powers supplied by the PFC converter and the grid being 11kW and 9 kW, respectively. The grid voltage is regulated to the nominal value, and Vpccd tracks it at 311V. The RMS value of the grid current, i_g, decreases from 63A to 41A, as shown in Fig. 16. At the steady-state period, the DC voltage ripple is approximately 17V, with an oscillation component at 100Hz.

The THD grid current at the steady-state period in Fig. 17 is 0.88% for this scenario, which complies with IEEE-519 standards with THD below 5%. This verifies the advantages of the IFB converter along with the IB-PWM technique.

3.4. Reactive Power Compensation

3.4.1. Power factor compensation

In this scenario, the system diagram comprises the grid, the IFB converter with an LC filter, and an RL load as shown in Fig. 18. The rated active and reactive power of the linear load is set at 11kW and 6.8kVar, respectively.

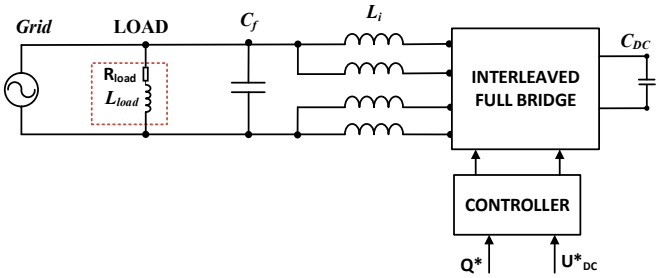

Fig. 18. System diagram for power factor compensation.

The start-up process and the system responses in this scenario are similar to those in the previous scenario. At 0.45 seconds, the RL linear load is connected to the circuit. In this case, the electrical grid is treated as an unlimited source; therefore, during the interval from 0.45s to 0.55s, both the load's active and reactive power are fully supplied by the grid. However, the reactive power demand of 6.8kW causes a phase difference between current and voltage, as shown in Fig. 19, resulting in the power factor falling below 0.85 and degrading the power quality of the electrical grid.

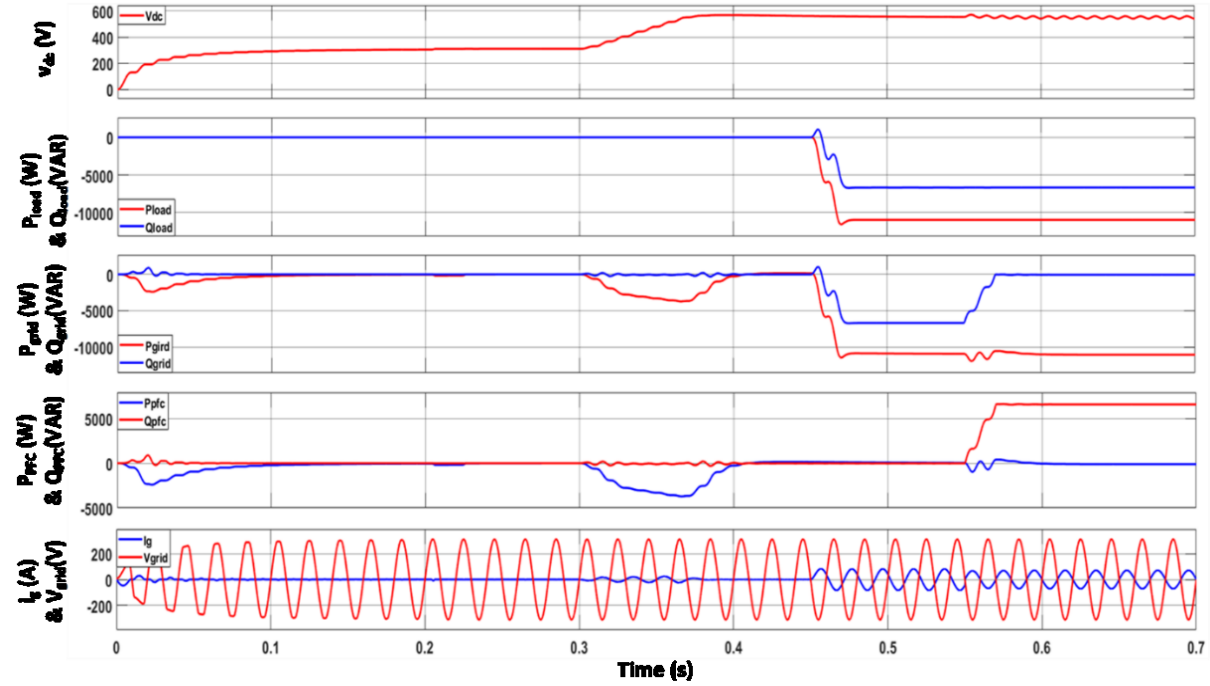

Fig. 19. System responses in the power factor compensation scenario.

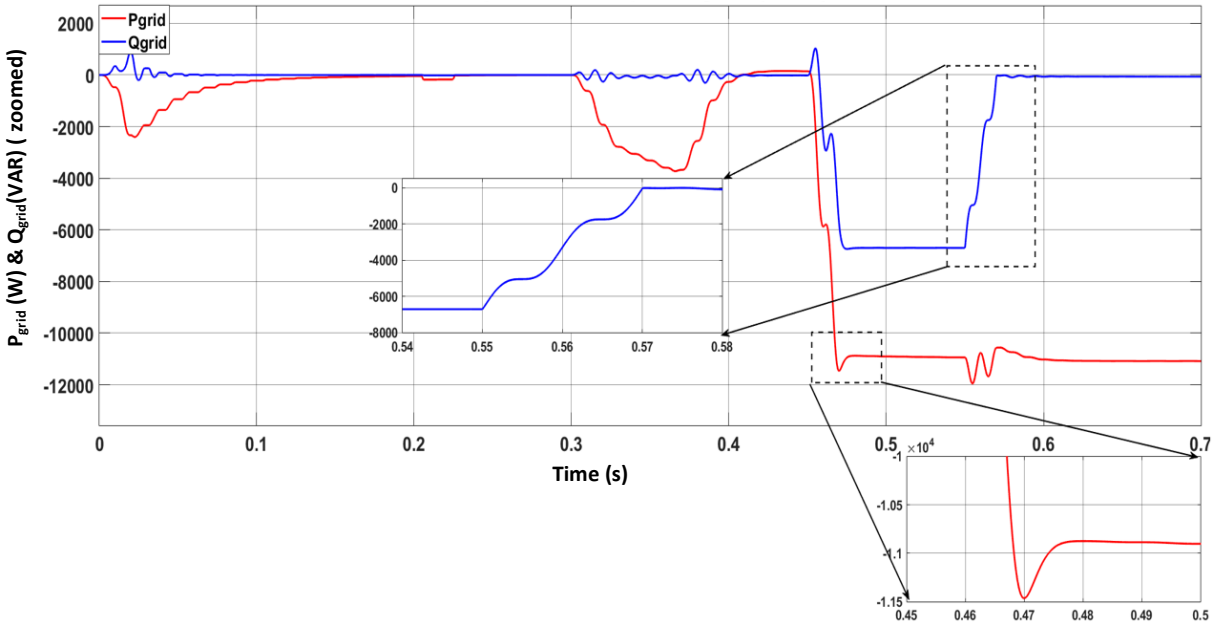

Fig. 20. Grid active and reactive power in a power factor compensation scenario.

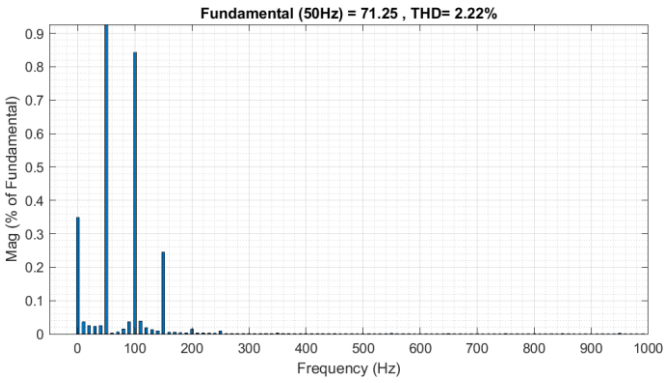

Fig. 21. THD current in power factor compensation.

At 0.55s, the IFB converter is initiated to compensate for reactive power in the grid. Due to the capability of independently controlling active and reactive power, the reference current i_{qr*} is calculated from the required load reactive power as in Eq. (4). Within 0.04s, the reactive power supplied by the IFB converter reaches 6.8kVAR as shown in Fig. 20, which is equal to the load reactive power. Simultaneously, as the reference active power of the PFC converter is zero, the grid supplies all the 11kW active power for the load. Therefore, the grid reactive power returns to zero as in Fig. 22, so the current becomes in phase with the grid voltage again, corresponding to a unity power factor. The response time is just one grid cycle, showing the effectiveness of the FAE technique.

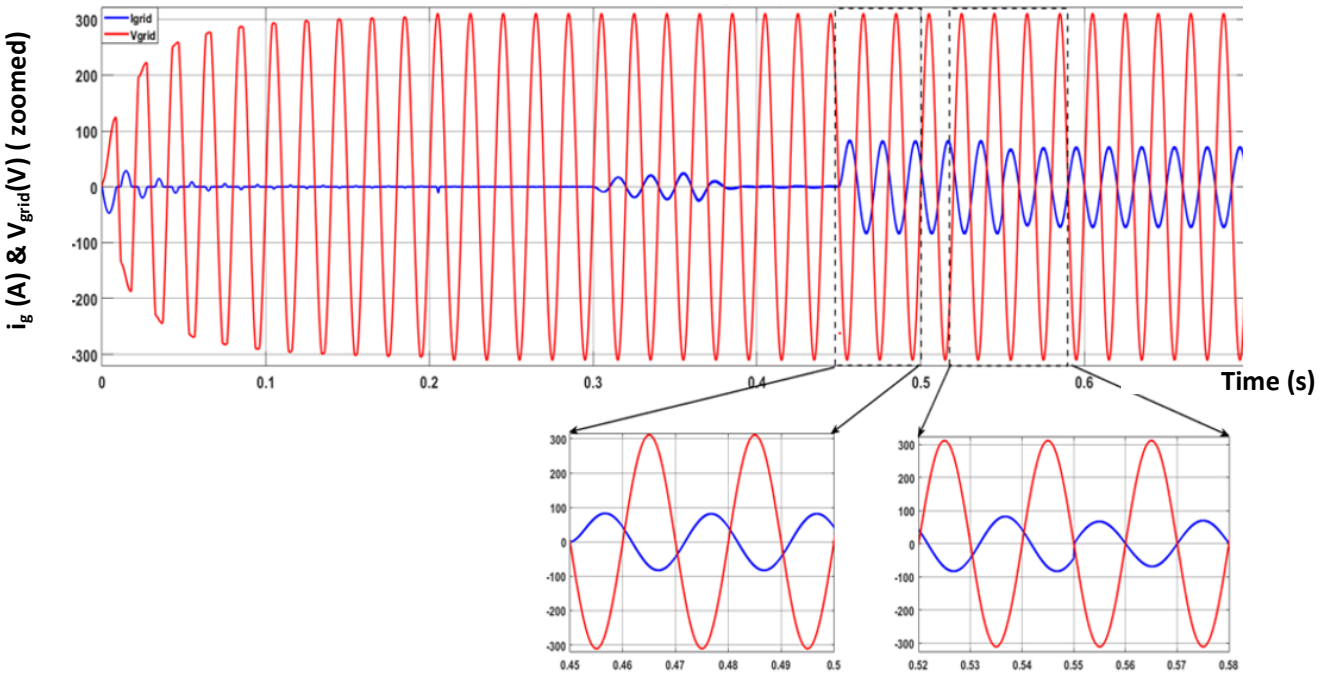

Fig. 22. Grid current and voltage responses in the power factor compensation scenario.

The THD of the grid current measured during the steady-state period in Fig. 21 is 2.22%, indicating the advantages of the IFB converter and the IB-PWM method. This THD value is below 5%, ensuring compliance with IEEE-519 standards.

3.4.2. PCC voltage regulation

In this scenario, the system diagram in Fig. 23 comprises the grid, the IFB converter with LC filter, and a resistive load of 5kW. The grid impedance is accounted for, with $R_g = 0.3\ \Omega$ and $L_g = 0.5\ mH$. Other simulation parameters are shown in Table 1. The start-up process from 0 to 0.45s is similar to the previous scenarios, as shown in Fig. 23. At 0.45s, the 5kW resistive load is connected to the PCC. Due to the impact of grid impedance as shown in Eq.(5), the PCC voltage rapidly drops to 295V after about 0.01 seconds as shown in Fig. 27

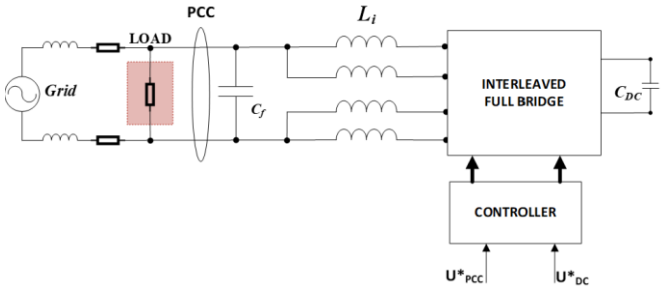

Fig. 23. System diagram for PCC voltage regulation.

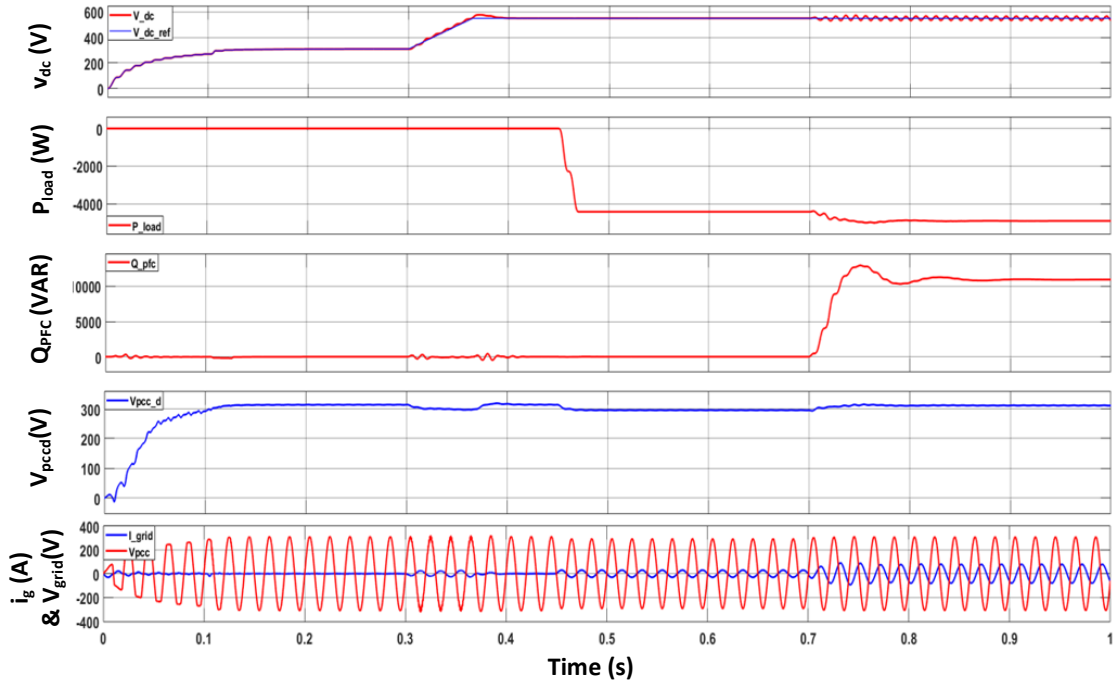

Fig. 24. System responses in PCC voltage regulation scenario.

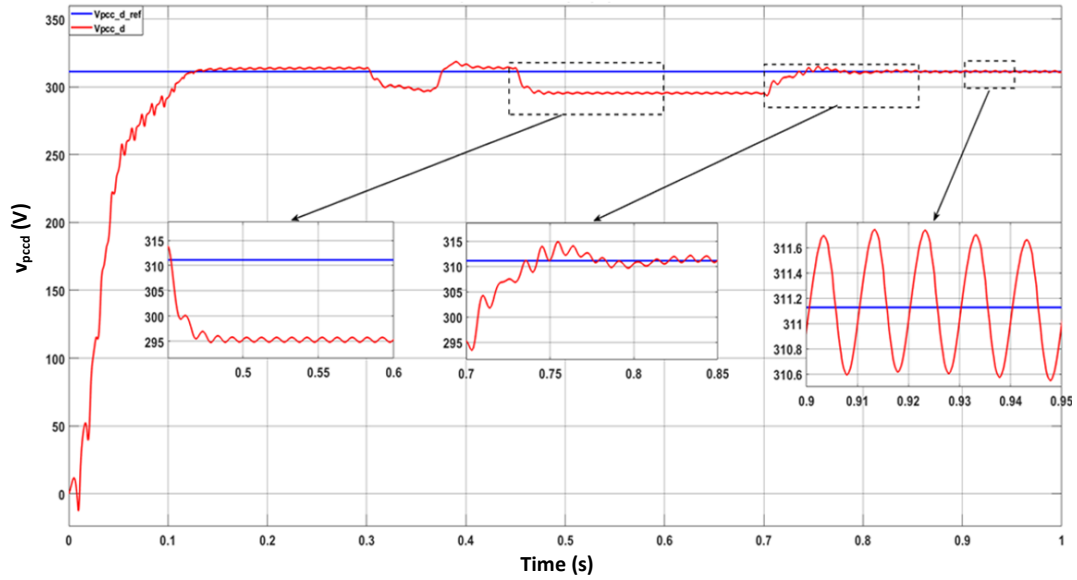

Fig. 25. Regulated PCC voltage.

At 0.7s, the IFB converter starts to operate with the PCC voltage controller. The q-axis reference current is calculated by the PCC voltage controller, as in Eq. (7), to compensate for approximately 11 kVAR of reactive power. The d-component PCC voltage V_{pccd} returns to its nominal value of 311V in about 0.1 seconds without overshoot. The THD grid current in Fig. 26 measured at the steady-state period is 1.23%, indicating the advantages of the IFB converter along with the IB-PWM method. This THD value is below 5%, ensuring compliance with IEEE-519 standards.

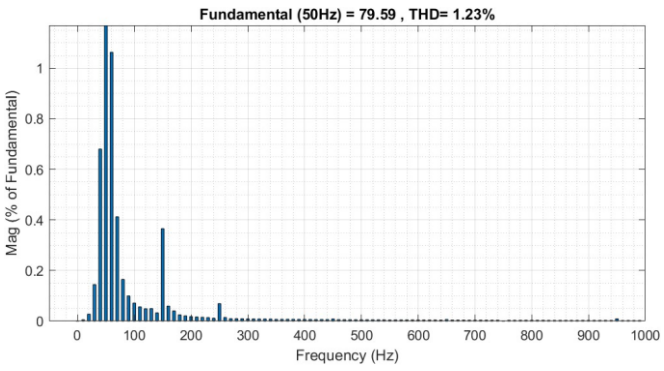

Fig. 26. THD current in the PCC voltage regulation case.

4. Conclusion

This paper proposes a novel P-Q control structure for the Interleaved Full Bridge (IFB) converter in a multifunctional AC Battery. One important task of a multi-functional AC Battery is to independently control active and reactive power, thereby supporting the grid in supplying power to domestic loads. Therefore, this paper proposed a single-phase PQ control scheme for the IFB converter to achieve this function. Additionally, the orthogonal current generated by a fictive-axis emulator is applied in the proposed control structure to improve the dynamic response of the current regulator and the overall system. To quickly verify the advantages of the IFB converter and the proposed control structure, real-time simulation using the Typhoon HIL platform is conducted in several scenarios: active power compensation, power factor compensation, and Point of Common Coupling (PCC) voltage regulation. The simulation results validate the efficiency of the control structure for the proposed converter in an AC Battery application.

Acknowledgment

This research is funded by the Hanoi University of Science and Technology (HUST) under project number T2022-TĐ-001.

Author Contributions:

Tuan Anh Do was responsible for conceptualization, validation, resource allocation, data curation, software development, and project administration. Quang Dich Nguyen and Phuong Vu jointly contributed to the methodology, formal analysis, investigation, original draft preparation, review and editing, visualization, supervision, and funding acquisition. All authors have read and agreed to the published version of the manuscript.

Conflict of Interest

The author(s) declared no potential conflicts of interest with respect to the research, authorship, and/or publication of this article.

References

[1] V. Smil, “The COP26 calls for impossibly steep cuts in carbon emissions: Numbers don't lie,” IEEE Spectrum, vol. 59, no. 2, pp. 20–21, Feb. 2022, doi: 10.1109/MSPEC.2022.9706399.

[2] J. Li, S. He, Q. Yang, Z. Wei, Y. Li and H. He, “A comprehensive review of second life batteries toward sustainable mechanisms: Potential, challenges, and future prospects,” IEEE Trans. Transportation Electrification, vol. 9, no. 4, pp. 4824–4845, Dec. 2023, doi: 10.1109/TTE.2022.3220411.

[3] C. Heymans, S. Walker, S. Young and M. Fowler, “Economic analysis of second use electric vehicle batteries for residential energy storage and load-levelling,” Energy Policy, vol. 71, pp. 22–30, 2014, doi: 10.1016/j.enpol.2014.04.016.

[4] K. Natesan and S. S. Prabhu, “Recent trends in lithium-ion battery – A critical review,” International Journal of Renewable Energy Research, vol. 12, no. 3, pp. 1506–1519, 2022, doi: 10.20508/ijrer.v12i3.13015.g8536.

[5] T. Tungjittrong and N. Teerakawanich, “Design and sizing of home PV/battery system with energy cost constraint using web application,” in Proc. 9th Int. Electrical Engineering Congress (iEECON), Pattaya, Thailand, 2021, pp. 129–132, doi: 10.1109/iEECON51072.2021.9440066.

[6] T. A. Do, Q. D. Nguyen, P. Vu, M. D. Ngo and S. J. Ahn, “Comparative analysis of PWM techniques for interleaved full bridge converter in an AC battery application,” Energies, vol. 17, p. 375, 2024, doi: 10.3390/en17020375.

[7] T. A. Do, Q. N. Le, T. L. Nguyen, N. Q. Dich and P. V. Hoang, “A new interleaved full-bridge converter for AC battery,” in Proc. 12th Int. Conf. Control, Automation and Information Sciences (ICCAIS), Hanoi, Vietnam, 2023, pp. 260–265, doi: 10.1109/ICCAIS59597.2023.10382330.

[8] T. A. Do, Q. D. Nguyen and P. Vu, “Design and implementation of a current-fed dual active bridge converter for an AC battery,” Journal of Electrical Engineering, vol. 75, no. 1, pp. 47–55, Feb. 2024, doi: 10.2478/jee-2024-0007.

[9] M. El and N. K. Bahgaat, “A comparison between using a firefly algorithm and a modified PSO technique for stability analysis of a PV system connected to grid,” International Journal of Smart Grid, vol. 1, no. 1, 2017.

[10] K. Okedu, “A variable speed wind turbine flywheel based coordinated control system for enhancing grid frequency dynamics,” International Journal of Smart Grid, vol. 2, no. 2.

[11] M. A. Tankari, D. Gueye and A. Ndiaye, “Design methodology of novel PID for efficient integration of PV power to electrical distributed network,” International Journal of Smart Grid, vol. 2, no. 1, Mar. 2018.

[12] A. N. Abed, H. H. Hussain and N. K. Kasim, “Performance analysis of grid-connected CIGS PV solar system and comparison with PVsyst simulation program,” International Journal of Smart Grid, vol. 3, no. 4, 2019.

[13] I. E. A. Davidson and E. Buraimoh, “Modelling of a photovoltaic-based grid supporting microgrid and fault ride-through control application,” International Journal of Smart Grid, vol. 7, no. 2, 2023.

[14] G. Wang and M. Bhardwaj, “6.6 kW three-phase interleaved totem pole PFC design with 98.9% peak efficiency for HEV/EV onboard charger,” in Proc. IEEE Applied Power Electronics Conf. and Exposition (APEC), Anaheim, CA, USA, 2019, pp. 2029–2034, doi: 10.1109/APEC.2019.8722110.

[15] M. Jauhari, A. F. Ilman, L. Prasetyani and T. Dewi, “Control strategy for active power filter based on P-Q theory under non-ideal mains voltages,” in Proc. 2nd Int. Conf. Industrial Electrical and Electronics (ICIEE), Lombok, Indonesia, 2020, pp. 31–35, doi: 10.1109/ICIEE49813.2020.9276891.

[16] M. Vimal and V. Sojan, "Vector controlled PMSM drive with power factor correction using zeta converter," in Proc. Int. Conf. Energy, Communication, Data Analytics and Soft Computing (ICECDS), Chennai, India, 2017, pp. 289–295, doi: 10.1109/ICECDS.2017.8389973.

[17] A. Alshalawi, H. Al-Barrak and M. Khalid, "P-Q control of microgrid with energy storage using adaptive controller," in Proc. Saudi Arabia Smart Grid (SASG), Riyadh, Saudi Arabia, 2022, pp. 1–7, doi: 10.1109/SASG57022.2022.10199799.

[18] L. Cheng, P. Xu, Q. Zhang and Y. Wang, "Improved PQ control method for PV system," in Proc. IEEE Symposium Series on Computational Intelligence (SSCI), Xiamen, China, 2019, pp. 2914–2920, doi: 10.1109/SSCI44817.2019.9002845.

[19] M. Azab, "Flexible PQ control for single-phase grid-tied photovoltaic inverter," in Proc. IEEE Int. Conf. Environment and Electrical Engineering and Industrial and Commercial Power Systems Europe (EEEIC/I&CPS Europe), Milan, Italy, 2017, pp. 1–6, doi: 10.1109/EEEIC.2017.7977550.

[20] G. M. Quintero, Y. R. Challapuram, A. Bilbao, S. B. Bayne, A. S. Subburaj and M. A. Harral, "Micro-grid system modeling efforts using PQ-control for single-phase and three-phase inverter," in Proc. IEEE Int. Telecommunications Energy Conf. (INTELEC), Turin, Italy, 2018, pp. 1–5, doi: 10.1109/INTLEC.2018.8612417.

[21] S. Samerchur, S. Premrudeepreechacharn, Y. Kumsuwun and K. Higuchi, "Power control of single-phase voltage source inverter for grid-connected photovoltaic systems," in Proc. IEEE/PES Power Systems Conf. and Exposition, Phoenix, AZ, USA, 2011, pp. 1–6, doi: 10.1109/PSCE.2011.5772504.

[22] B. Bahrani, A. Rufer, S. Kenzelmann and L. A. C. Lopes, "Vector control of single-phase voltage-source converters based on fictive-axis emulation," IEEE Transactions on Industry Applications, vol. 47, no. 2, pp. 831–840, Mar.–Apr. 2011, doi: 10.1109/TIA.2010.2101992.

[23] A. Khaligh and S. Dusmez, "Comprehensive topological analysis of conductive and inductive charging solutions for plug-in electric vehicles," IEEE Transactions on Vehicular Technology, vol. 61, no. 8, pp. 3475–3489, Oct. 2012, doi: 10.1109/TVT.2012.2213104.

[24] F. Taghizadeh, M. J. Hossain, J. Lu and W. Water, "A unified multi-functional on-board EV charger for power-quality control in household networks," Applied Energy, vol. 215, pp. 186–201, 2018, doi: 10.1016/j.apenergy.2018.02.006.

[25] A. Yazdani and R. Iravani, Voltage-Sourced Converters in Power Systems. Hoboken, NJ, USA: Wiley/IEEE Press, 2010.

[26] B. K. Perera, P. Ciufo and S. Perera, "Point of common coupling (PCC) voltage control of a grid-connected solar photovoltaic system," in Proc. IECON 2013 – 39th Annual Conf. IEEE Industrial Electronics Society, Vienna, Austria, 2013, doi: 10.1109/IECON.2013.6700377.